ACS OMEGA

Open Access

http://pubs.acs.org/journal/acsodf

Article

Phase-Dependent Properties of Manganese Oxides and Applications in Electrovoltaics

Hira Batool, Abdul Majid,* Sheraz Ahmad, Adil Mubeen, Mohammad Alkhedher, Waseem Sharaf Saeed, Ahmad Abdulaziz Al-Owais, and Aqeel Afzal

Cite This: *ACS Omega* 2024, 9, 2457−2467

Read Online

ACCESS | Metrics & More | Article Recommendations | Supporting Information

ABSTRACT: This study reports first-principles predictions as well as experimental synthesis of manganese oxide nanoparticles under different conditions. The theoretical part of the work comprised density functional theory (DFT)-based calculations and first-principles molecular dynamics (MD) simulations. The extensive research efforts and the current challenges in enhancing the performance of the lithium-ion battery (LIB) provided motivation to explore the potential of these materials for use as an anode in the battery. The structural analysis of the synthesized samples carried out using X-ray diffraction (XRD) confirmed the tetragonal structure of Mn_3O_4 on heating at 450 and 550 °C and the cubic structure of Mn_2O_3 on heating at 650 °C. The structures are found in the form of nanoparticles at 450 and 550 °C, but at 650 °C, the material appeared in the form of a nanoporous structure. Further, we investigated the electrochemical functionality of Mn_2O_3 and Mn_3O_4 as anode materials for utilization in LIBs via MD simulations. Based on the investigations of their electrical, structural, diffusion, and storage behavior, the anodic character of Mn_2O_3 and Mn_3O_4 is predicted. The findings indicated that 10 lithium atoms adsorb on Mn_2O_3, whereas 5 lithium atoms adsorb on Mn_3O_4 when saturation is taken into account. The storage capacities of Mn_2O_3 and Mn_3O_4 are estimated to be 1697 and 585 mAh g^{-1}, respectively. The maximum value of lithium insertion voltage per Li in Mn_2O_3 is 0.93 and 0.22 V in Mn_3O_4. Further, the diffusion coefficient values are found as 2.69×10^{-9} and 2.65×10^{-10} m^2 s^{-1} for Mn_2O_3 and Mn_3O_4, respectively, at 300 K. The climbing image nudged elastic band method (Cl-NEB) was implemented, which revealed activation energy barriers of Li as 0.30 and 0.75 eV for Mn_2O_3 and Mn_3O_4, respectively. The findings of the work revealed high specific capacity, low Li diffusion energy barrier, and low open circuit voltage for the Mn_2O_3-based anode for use in LIBs.

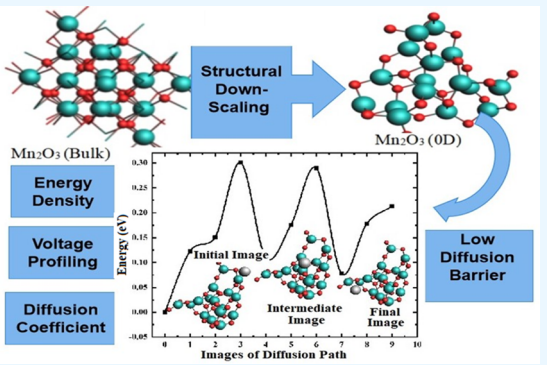

1. INTRODUCTION

There have been unprecedented research efforts to produce efficient and sustainable energy devices in the recent past. The anticipated large-scale utilization of electric vehicles in the near future demands lightweight, low-cost, high energy density, and efficient energy storage devices. Lithium-ion batteries (LIBs) have been among the best-known solutions in this regard to meet the impending issues of energy crises, depletion of nonrenewable fuels, environmental degradation due to conventional batteries, and rising demand for clean energy. Despite remarkable successes including reasonably high energy density, long life cycle, and good rate capability, the research efforts to improve the performance of LIBs are still at the heart of research related to energy devices.[1,2] Graphite is the most commonly used anode material employed in LIBs that offers a theoretical capacity of 372 mAh g^{-1}.[3,4] The utilization of nanostructured materials for use as electrodes in LIBs has been extensively investigated in the recent past.[5] However, these materials have been found suffering from structural degradation, low electrical conductivity, and significant volume change during lithium intercalation/deintercalation, leading to subpar cyclic performance of the battery.[6]

The inferior performance of current LIBs and future technological requirements demand the fabrication of economical and high storage capacity batteries. The research efforts in this regard produced favorable outcomes in the form of graphite-alternate electrodes such as silicon, germanium, tin, and carbon nanotubes. The batteries comprising such materials face issues related to capacity fading, structural stability, volume expansion, and thermal management during charging and discharging.[7−9] The improved electrochemical performance of these materials has been attributed to hollow-shaped nanomaterials with unique properties.[10] The hollow nano-

Received: September 11, 2023
Revised: December 13, 2023
Accepted: December 15, 2023
Published: January 3, 2024

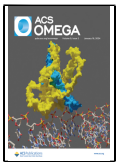

structure can improve the properties of lithium storage by allowing a significantly reduced diffusion path for lithium ions by increasing the electrode's area of contact for Li intercalation and deintercalation. Further, it provides additional free volume to reduce structural strain during charge/discharge cycles.[11,12]

The preparation of new electrode materials based on the alloying of silicon, phosphorus, and tin has been a strategy to exhibit higher values of storage capacity. The theoretical capacities of carbon are 372 and 830 mAh g^{-1}, respectively, while silicon, phosphorus, and tin have extremely high specific capacities of 4007, 2596, and 959 mAh g^{-1} and very high volumetric capacities of 9330, 6982, and 7066 mAh cm^{-3}, respectively.[13] Many studies have been conducted to prepare novel electrode materials in the form of nonporous and nanotube architectures for improving the functioning of LIBs. The material engineering of nanostructures offers ways to improve performance by enhancing the rate capability and storage capacity. In the case of nanostructures, the distance across which Li^+ must diffuse in the solid state is reduced, which encourages the utilization of such materials for electrodes in LIBs. The low-cost nanoscale materials have been predicted for use as an anode in order to prepare economical, ecologically friendly, highly efficient, and functional LIBs.[14]

The experimental synthesis of ruthenium oxide nanoplates, followed by ex situ lithiation in line with the theoretical predictions of these materials, has proven to be beneficial for conducting meaningful research and gaining a better understanding of the complex mechanisms involved.[15−17] The integration of computational and synthesis methodology by bridging the gap between corresponding theory and experimental schemes has been found helpful in shedding light on the potential of ruthenium oxide nanoplates as cutting-edge anode materials. The synergistic approach to simultaneously utilize the experimental synthesis and first-principles computations to investigate the lithiation mechanism in $W_{18}O_{49}$ has been found advantageous.[18] This study has been helpful to shed light on the material's electrochemical behavior during charge/discharge cycles by revealing the fundamental interactions between the matrix and lithium ions. Further, the recent upgradation of computational resources has made efficient theoretical predictions possible to facilitate the experimental synthesis of new materials. The synergistic methods are thus found very helpful in expanding our knowledge on electrode materials and their utilization in designing high-performance LIBs.

The nanomaterials have been found to offer exceptionally high surface energies, which improve their electrochemical, electronic, and transport properties. It is envisaged that high-energy-density electrode materials can be created by using nanomaterials to improve battery performance. This study is dedicated to exploring the structural, electronic, and transport properties of Mn_2O_3- and Mn_3O_4-based nanomaterials for application as anodes in LIBs. The study was carried out by experimentally synthesizing the materials using chemical routes and density functional theory (DFT)-based first-principles simulations.

2. METHODOLOGY

The work was carried out using experimental methods (given in the Supporting Information) and first-principles-based theoretical strategies in the following.

The Amsterdam density function (ADF) BAND and DFTB modules were used to implement all of the density functional theory (DFT)-based calculations.[14] The Perdew−Burke−Ernzerhof (PBE) functional was used with the generalized gradient approximation (GGA) to handle exchange−correlation interactions,[18] taking into account the van der Waals interactions in the host materials Mn_2O_3 and Mn_3O_4, and the dispersion-corrected Grimme D3 technique was used.[19] The structure is optimized using the quasi-Newton method.[20] In order to achieve the optimized geometry of the structures, the energy convergence threshold was set at 1×10^{-5} Ha with full relaxation of atomic positions until the force gradient was less than 0.02 eV, with a step size of 0.001 eV and 8 *K*-points. In order to perform the calculations, the triple zeta-polarized (TZP) fundamental function from ADF-BAND was used. Becke fuzzy cell integration and the frozen core approximation were utilized to set the numerical quality to be good.

The first-principles computations on Mn_2O_3 and Mn_3O_4 under periodic boundary conditions are described in this study, beginning with 28 atoms with lattice constants $a = b = 5.74$ Å, $c = 9.41$ Å. To develop zero-dimensional nanostructures, the initial configuration of the materials was taken from the bulk structures and then downscaled to obtain the optimized models. We were able to achieve the targeted nanostructure while maintaining the structural characteristics and fundamental properties of the materials. The minimum energy configurations of these downscaled structures were obtained using complete geometric optimization, ensuring the accuracy and stability of the materials for subsequent calculations. This strategy and the employed computational details provided a foundation to correctly predict the properties of the prepared nanostructures.

The nanostructures of Mn_2O_3 and Mn_3O_4 were then optimized. In order to find the chemical potential, the metallic phase of Li with the BCC structure was also optimized. A single Li atom was positioned in the host structures Mn_2O_3 and Mn_3O_4 at different symmetry locations to conduct energy profiling. We identified favorable adsorption sites in the structures of Mn_3O_4 and Mn_2O_3 to introduce Li atoms. This process allowed us to determine energetically suitable lithium configurations in the hosts and subsequently placed lithium atoms on the sites to optimize their positions for the accurate simulation of the lithiation process.

The lithiation mechanism of Mn_2O_3 and Mn_3O_4 can be defined using eq 1[21−23]

$$Mn_aO_b + (b{\cdot}n)Li^+ + (b{\cdot}n)e^- \leftrightarrow a\ Mn + b\ Li_nO \quad (1)$$

where a and b are the stoichiometries of Mn_aO_b and n is the stoichiometry of Li_nX. The predicted lithium-ion storage capacity of Mn_2O_3 is higher than that of Mn_3O_4 due to distinct manganese oxidation states. Mn_2O_3 primarily consists of manganese in the +3 oxidation state (Mn^{3+}), while Mn_3O_4 contains a combination of Mn^{2+} and Mn^{3+} ions with +2 and +3 oxidation states, respectively. Mn^{3+} ions in Mn_3O_4 contribute to the lithium storage capacity, as they can accept lithium ions during charging. However, the presence of Mn^{2+} ions in the structure limits the overall capacity because Mn^{2+} ions cannot accept as many lithium ions as Mn^{3+} ions due to their lower charge (+2). Mn_2O_3 can accommodate more lithium ions per unit of manganese because it has only Mn^{3+} ions with a higher charge (3+) compared to Mn_3O_4, which also has Mn^{2+} ions (2+) along with Mn^{3+} ions (3+). The difference in the oxidation states of manganese in Mn_2O_3 (Mn^{3+}) and Mn_3O_4

https://doi.org/10.1021/acsomega.3c06913
ACS Omega 2024, 9, 2457−2467

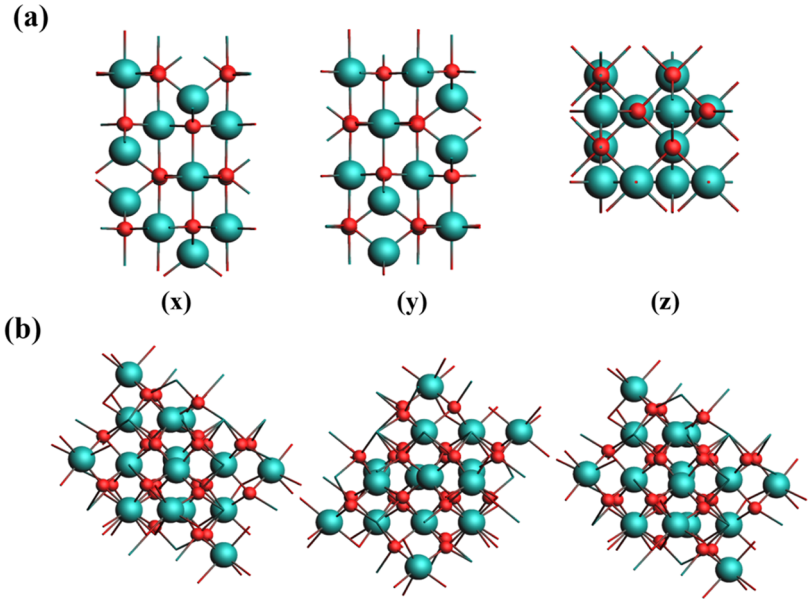

Figure 1. Optimized structures of (a) Mn_3O_4 (bulk) and (b) Mn_2O_3 (bulk) along all possible directions.

(Mn^{2+} and Mn^{3+}) is a key factor influencing their lithium-ion storage capacities. Mn_2O_3, with its higher charge per manganese ion, can theoretically store more lithium ions per unit mass, making it have a higher capacity compared to Mn_3O_4.[24−26]

By relaxing the geometry and utilizing the energy difference between lithiated and delighted structures, the calculations are carried out to determine the favorable site for lithium intercalation.[27] The process of lithiation is taken into account when lithiation energy is negative, which refers to an exothermic reaction.[28] The sites in the host structure with the higher negative lithiation energy value are designated as the most favorable sites and are capable of hosting more Li atoms to search for the enhanced concentration of Li. The value of lithiation energy is calculated using eq 2[29]

$$E_{\text{lithiation}} = (E_{\text{Li}_x\text{host}} - xE_{\text{Li}} - E_{\text{host}})/x \tag{2}$$

where E_{ad} is the adsorption energy (eV), $E_{\text{Li}(x)\text{host}}$ is the total energy following the adsorption of lithium in the host (Mn_2O_3 or Mn_3O_4 in this study), E_{host} is the optimized energy of the host prior to the adsorption of lithium, and E_{Li} is the energy of a single lithium atom. The value of x gives the number of lithium atoms in the structure.

The main criterion for choosing an anode in LIBs is its storage capacity, which can be calculated using eq 3[30]

$$C = \frac{x \times F}{M_{\text{host}}} \tag{3}$$

where F is Faraday's constant, having a value of 26.801 Ah/mol, x is the number of lithium atoms used in the simulation,[31] and M_{host} is the molecular weight of the host structure Mn_2O_3 or Mn_3O_4.

To test the performance of Mn_2O_3 and Mn_3O_4 as anodes, calculations are performed for voltage profiling using eq 4[32,33]

$$V = \frac{E_{\text{Li}_{x2}\text{host}} - E_{\text{Li}_{x1}\text{host}} - (x_2 - x_1)E_{\text{Li}}}{(x_1 - x_2)e} \tag{4}$$

where $E_{\text{Li}_{x2}\text{host}}$ and $E_{\text{Li}_{x1}\text{host}}$ are the energies of $\text{Li}_{x2\text{host}}$ and $\text{Li}_{x1\text{host}}$, respectively, E_{Li} represents the chemical potential of lithium, and e is the electronic charge.

Molecular dynamics (MD) simulations offer a resourceful computational tool to explore the intricate dynamics of atoms and molecules in a variety of structures. These simulations are particularly instrumental in elucidating the behavior of systems to bridge the gap between theory and experimentation. In the context of an NTV ensemble, which maintains a constant number of particles, temperature, and volume, it has emerged as a reliable framework for simulating molecular systems under realistic conditions. The MD calculations were conducted at various temperatures within the canonical ensemble NTV. Throughout the simulations for unfolded trajectories, we determined the mean square displacement (MSD), which describes the particle's distance from a reference point at regular intervals of 0.25 fs. Subsequently, we calculated the MSD and diffusion coefficient using eqs 5 and 6, respectively.

$$\text{MSD} = \langle |r(t) - r(0)|^2 \rangle \tag{5}$$

$$D(T) = D_0 \exp - \left(\frac{E_a}{kT}\right) \tag{6}$$

In this context, "$r(0)$" signifies the initial position, while "$r(t)$" corresponds to the particle's ultimate location. We computed the diffusion coefficients for lithium over a temperature range spanning 300 to 800 K and depicted the Arrhenius relationship of D as a function of $1/T$.

In order to investigate lithium's minimal energy path in hosts Mn_2O_3 and Mn_3O_4, a nudged elastic band (CI-NEB) was used with eight intermediate images.[34] The spring constant value was set at 1.0 Ha/Bohr^2, and skewness was set to 1.0.[35] To avoid image overlapping, global optimization was used rather than local optimization.[36] Spring forces were pooled rather than taking into consideration the parallel forces along the reaction channel with the force determined using eq 7[37]

$$F_i = |F_i^s|_{\parallel} - |\nabla E(R_i)|_{\perp} \tag{7}$$

https://doi.org/10.1021/acsomega.3c06913
ACS Omega 2024, 9, 2457−2467

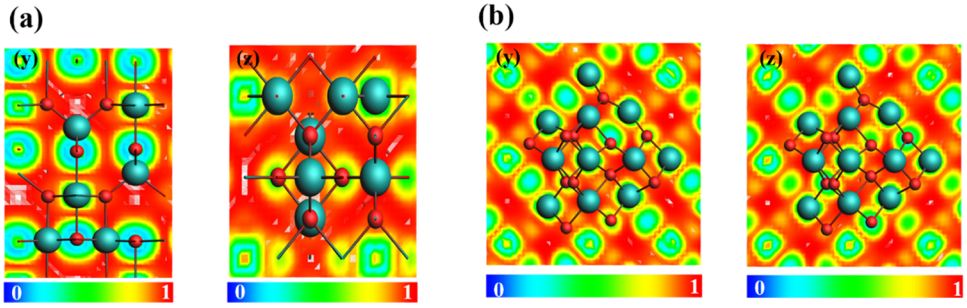

Figure 2. ELF plot of (a) Mn_3O_4 (bulk) and (b) Mn_2O_3 (bulk) along the *y*-axis and *z*-axis.

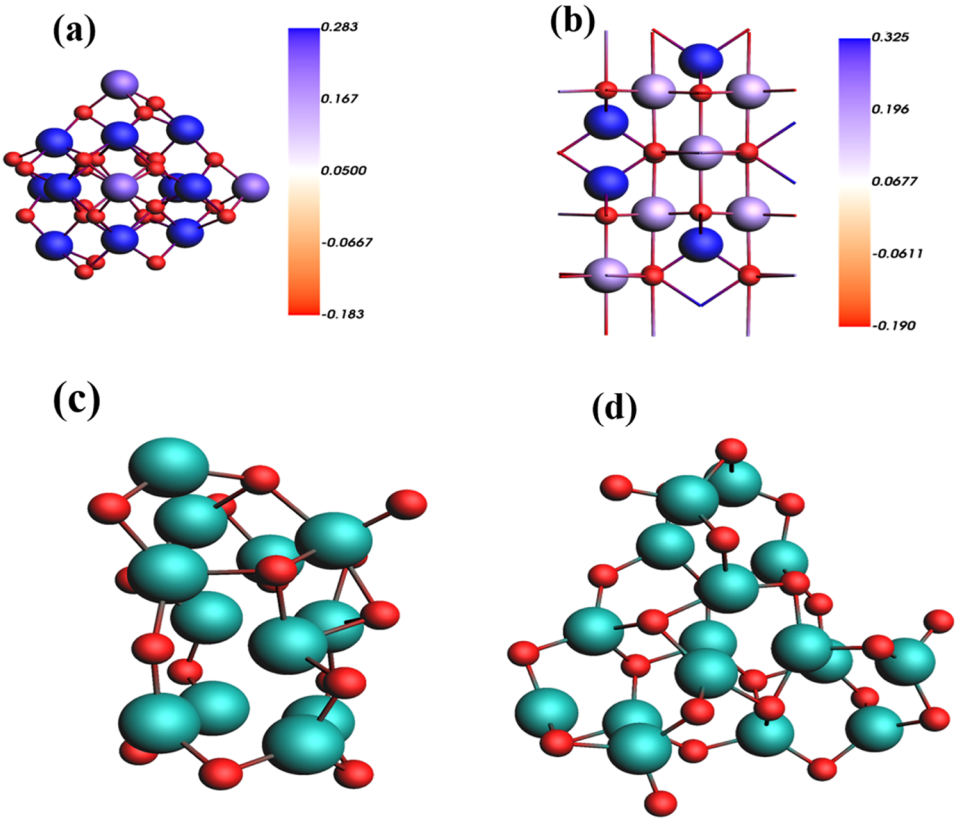

Figure 3. Hirshfeld analysis of (a) Mn_2O_3 (bulk) and (b) Mn_3O_4 (bulk). Optimized structures of (c) Mn_3O_4 (0D) and (d) Mn_2O_3 (0D).

where F_i is the sum of all forces on the *i*th image, $|F_i^s|_{||}$ is the spring force, and $|\nabla E\ (R_i)|_\perp$ is the true force. The maximum energy image is found in eq 8.

$$F_{i\max} = \nabla E(R_{i\max}) + 2\nabla E\,|R_{i\max}|_{||} \tag{8}$$

Different transition paths were taken into account in the simulation, out of which only two paths with the minimum transition barrier were reported.

3. RESULTS AND DISCUSSION

3.1. Structural Properties. Bulk Mn_3O_4 exhibits a tetragonal structure with the space group $I4_1/amd$, and optimized lattice constants are a = 5.74 Å, c = 9.42 Å, and α = 90° that agree well with reported experimental values (a = 5.76 Å, c = 9.44 Å, and α = 90°). The unit cell consists of 14 atoms, including 6 Mn atoms and 8 O atoms, in such a way that each Mn is bound to four O atoms to form a MnO_4 tetrahedron that shares corners with 12 MnO_6 octahedrons.[38] The Mn−O bond length is 2.0 Å. On the other hand, bulk Mn_2O_3 exhibits a cubic structure with the space group $Ia3^-$, and optimized lattice constants are $a = b = c$ = 4.17 Å and $\alpha = \beta = \gamma$ = 90°. Its unit consists of 40 atoms, 16 Mn atoms, and 24 O atoms. In the initial Mn^{3+} site, Mn^{3+} is connected to six identical O^{2-} atoms, creating a combination of MnO_6 octahedra that share both edges and corners. The Mn−O bond length is 1.93 Å. Figure 1 represents the view of the Mn_3O_4 and Mn_2O_3 structures in different directions.

3.2. Bonding Analysis. The electron localization function (ELF) is a valuable tool for analyzing electronic structure and delocalization in solids to describe the bonding characteristics of the materials.[39] ELF offers values between 0 and 1 in such a way that the value of 1 signifies perfect electron localization, while ELF = 0.5 indicates full electron delocalization. The minimum ELF value, ELF = 0, represents a low charge density. In the context of Mn_3O_4, as shown in Figure 2a, a distinct electron localization surrounding the O atom is observed. However, a red region (ELF = 0) is observed around the Mn atoms, which points to electron deficiency. This observation

https://doi.org/10.1021/acsomega.3c06913
ACS Omega 2024, 9, 2457−2467

suggests the presence of significant ionic bonding characteristics in the Mn−O bonds. In the meantime, the Hirshfeld analysis shown in Figure 3b reveals a substantial charge transfer of 0.33e from each Mn atom to the O atom. These findings further substantiate the ionic bonding nature of the Mn−O bonds. The material was then structurally downscaled to 0D, and the optimized structure is shown in Figure 3c. The Mn−O bond length for 0D is calculated as 1.94 Å.

In the case of Mn_2O_3 (Figure 2b), distinct electron localization via the area surrounding the O atom is evident. However, a red-colored region (ELF = 0) is observed around the Mn atoms, indicating electron deficiency. This observation suggests the presence of significant ionic bonding characteristics in the Mn−O bonds. In the meantime, the Hirshfeld analysis shown in Figure 3a reveals a substantial charge transfer of 0.28*e* from each Mn atom to the O atom. These findings further substantiate the ionic bonding nature of the Mn−O bonds. The material was downscaled to 0D, and the optimized structure is shown in Figure 3d. The Mn−O bond length for 0D is calculated as 1.73 Å.

To analyze the structural stability of MnO-based compounds in bulk and 0D, the formation energy is calculated using eq 9

$$E_{form} = \frac{xE_{Mn} - yE_O - E_{Mn_xO_y}}{x + y} \quad (9)$$

where E are respective energies, and x and y are the numbers of corresponding atoms.

In order to check the stability of Mn_3O_4, we calculated the formation energy, which appeared as 1.35 eV per atom, and similarly, for 0D, it was found to be 1.20 eV. The reported values of formation energies of FeO, Fe_2O_3, K_2O, and Sb_2O_3 are 2.82, 8.56, 3.76, and 3.39 eV, respectively.[40−42] The formation energy estimation provided clear evidence that Mn_3O_4 was a stable structure.

Similarly, the calculated value of formation energy in the case of Mn_2O_3 appeared as 1.52 eV per atom, and for 0D, it is calculated as 1.45 eV. To explain the trend in MnO-based compounds, the phase diagram is shown in Figure 4. The formation energy is a parameter that serves as an indicator of a compound's thermodynamic stability, where a lower formation energy suggests higher stability. The minima on the diagram represent the most stable compounds or phases for particular compositions, essentially revealing which compounds are preferred at specific atomic fractions. The phase diagram indicates that Mn_2O_3 is more stable as compared to Mn_3O_4, so phase change is probable under specific conditions.

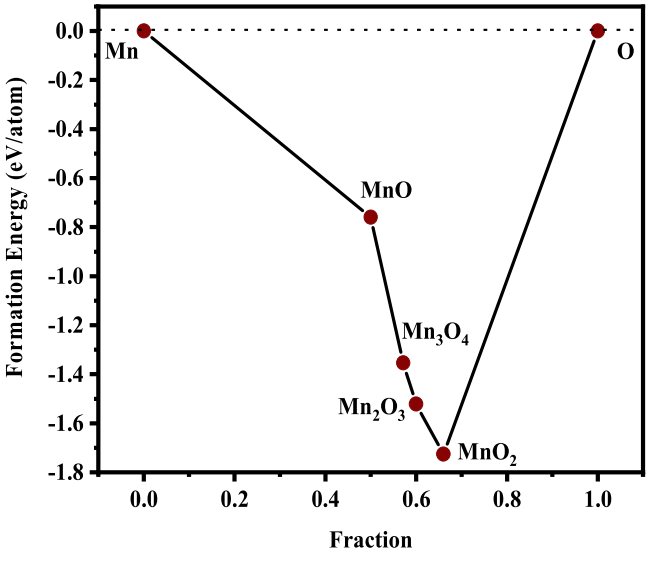

Figure 4. Phase diagram of MnO as a function of atomic fraction.

3.3. Electronic Properties. In order to investigate the electronic properties of Mn_3O_4, we calculated its band structure at the PBE level by adding Hubbard (DFT + U) correction.[43−45] Figure 5 indicates that Mn_3O_4 in bulk possesses an indirect band gap of 0.092 eV. Since the PBE functional tends to underestimate band gaps, an alternative calculation was performed using the TB-mBj level of theory, known for its accuracy in describing electron correlation energies in various solids.[46] The band diagram of bulk Mn_3O_4, as calculated by TB-mBj, is presented in Figure 5b, revealing a band gap of 0.80 eV. The density of states (DOS) with the presence of spin-restricted effects is shown in Figure 6. The TDOS plots show that there is a clear difference between spin-up and spin-down states, exhibiting spin polarization around the Fermi level, which suggests the magnetic behavior of the material. Further, upon observing electronic configuration for Mn and O, respective electronic configurations are [Ar] $3d^5$, $4s^2$ and $1s^2$, $2s^2$, $2p^4$. The d orbitals of Mn and p orbitals of O clearly form conduction and valence bands according to the electronic configuration, which is consistent with the PDOS of Mn_3O_4 shown in Figure 6b. Therefore, Mn d and O p states are the reason for the majority of the DOS at the near Fermi level in the valence band and the reason for p−d hybridization along higher energy levels, while in the conduction band, the majority of the Mn d states contribute to the spin-down region and very small contribution comes from O p states. Figure 6b makes it clear that the spin-up and spin-down channels of the total density of states (PDOS) are asymmetric and consistent with TDOS results, suggesting that Mn_3O_4 has the properties of a magnetic ground state.

3.4. Phase Change. To investigate the phase of the materials, molecular dynamics (MD) simulations were conducted under the NVT ensemble framework, employing a time step of 0.25 fs and maintaining a temperature of 450, 650, and 950 K. The temperature was controlled using the Nose−Hoover chain (NHC) thermostat. The equilibration of Mn_3O_4 was achieved over a duration of 6 ps through 25,000 simulation steps.[47] The MD simulations were carried out at 450 and 650 K, spanning a time evolution of 25 ps. Throughout this simulation, no deformations or bond breakages in the structure are observed, which points to the excellent thermal stability of Mn_3O_4.

In Figure 7a,b, temperature and energy profiles at 450 and 950 K are plotted against the time steps. Figure 7c presents snapshots captured at intervals of 170 ps during the MD simulation, providing insights into the simulation's progress. Notably, after the initial 20 ps, the overall energy of the structure remained nearly constant. Upon concluding the simulation, it becomes evident that the Mn_3O_4 structure (0D) changes the phase to Mn_2O_3. In the new structure, two Mn^{3+} sites are inequivalent. Mn^{3+} is bound to six corresponding O^{2+} atoms at the initial Mn^{3+} site to form a mixture of edge- and corner-sharing MnO_6 octahedra. The second Mn^{3+} site is a mixture of deformed edge and corner-sharing MnO_6 octahedra, where Mn^{3+} is linked to six equiv O^{2-} atoms. The Mn−O bond distances range from 1.63 to 1.74 Å.

https://doi.org/10.1021/acsomega.3c06913
ACS Omega 2024, 9, 2457−2467

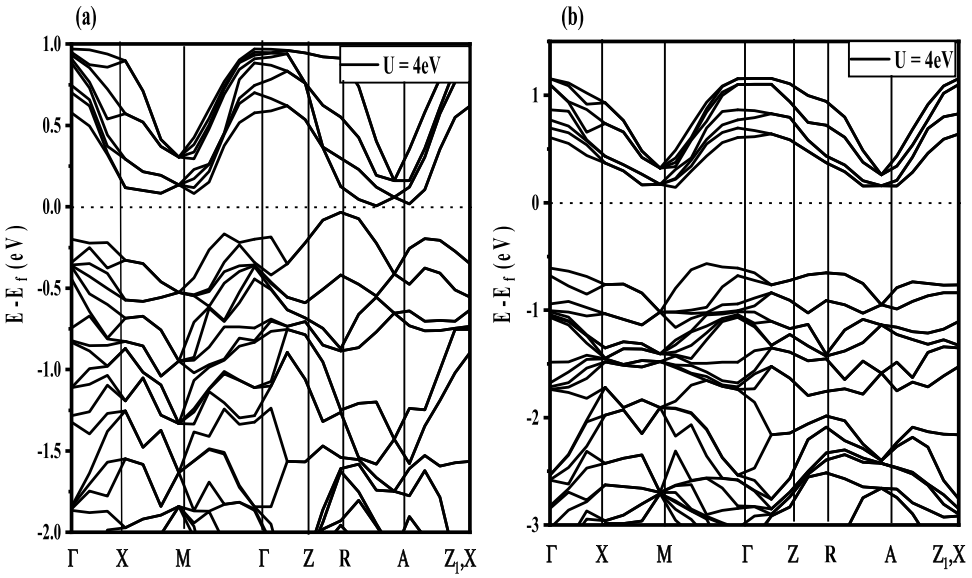

Figure 5. Calculated band diagram of Mn_3O_4 (bulk): (a) band structure with GGA-PBE + *U* and (b) TB-mBj + *U*. The Fermi level is adjusted to 0 eV.

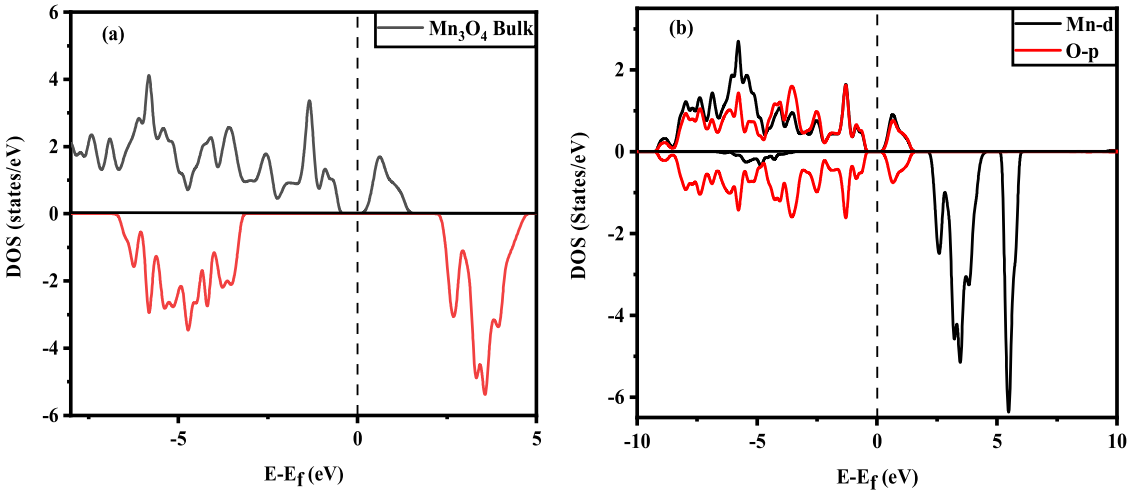

Figure 6. Calculated DOS of Mn_3O_4 (bulk): (a) TDOS with TB-mBJ + *U* and (b) PDOS. The Fermi level is adjusted to 0 eV.

3.5. Experimental Validation of Phase Change. The data are provided in the Supporting Information of the manuscript.

3.6. Lithiation Energy. The concentration of the Li atom in the host material was steadily increased in order to calculate storage capacity. Li atoms are permitted to interact with the host structures Mn_2O_3 and Mn_3O_4 in the fully optimized environment to occupy a stable position. The calculated optimum energy values are used to monitor the nature of the reaction and to determine the lithiation energies at various Li concentrations. The host structures did not significantly distort as Li concentration was increased, which indicates the durability of the host structure to resist deformation. The computed values of lithiation energy as a function of lithium concentration are shown in Figure 8. The value of the lithiation energy increases linearly with an increase in Li concentration for both host materials. At 10 Li atom adsorption in Mn_2O_3, the value of lithiation energy remains in the negative region, resulting in an exothermic reaction, and lithiation energy reaches its maximum value. This is due to the fact that at 10 Li atom adsorption, the maximum charge transfer occurs. Following this, the lithiation energy continues to rise until there are 10 Li atoms, at which point the process is still exothermic. The value turns positive, and the reaction shifts to an endothermic state with the addition of 11 Li atoms. For the case of Mn_3O_4, the reaction remains exothermic until 5 Li atom intercalation when we increase the Li from 5 atoms to 6 atoms, the system turns out to be endothermic, and the reaction is no more favorable.

The value of storage capacity calculated using eq 3 with various Li concentrations in the host is depicted in Figure 9, and the capacities of Mn_2O_3 and Mn_3O_4 matrices turned out to be 1697.66 and 585.67 $mAhg^{-1}$, respectively, with 10 and 5 Li intercalation within the limit of an exothermic reaction.

3.6.1. Graphite Capacity. Since graphite is a commonly used electrode in LIBs, we utilized it as a benchmark material to assess the reliability of Mn_2O_3 and Mn_3O_4. The calculations conducted for this work identified several crucial characteristics of the proposed material that make it preferable to graphite. In the case of Mn_2O_3 and Mn_3O_4, an exothermic reaction was

https://doi.org/10.1021/acsomega.3c06913
ACS Omega 2024, 9, 2457−2467

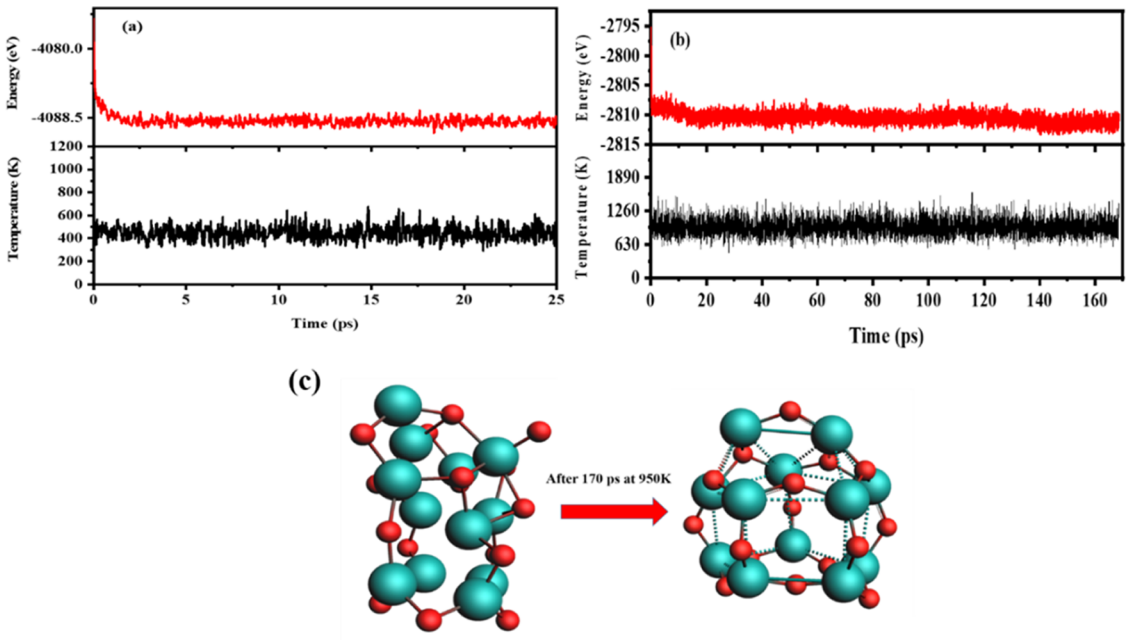

Figure 7. MD simulations showing temperature as a function of time for Mn_3O_4 (0D) at (a) 450 K and (b) 950 K (c) The snapshot of molecular dynamics simulations recorded after 170 ps for Mn_3O_4.

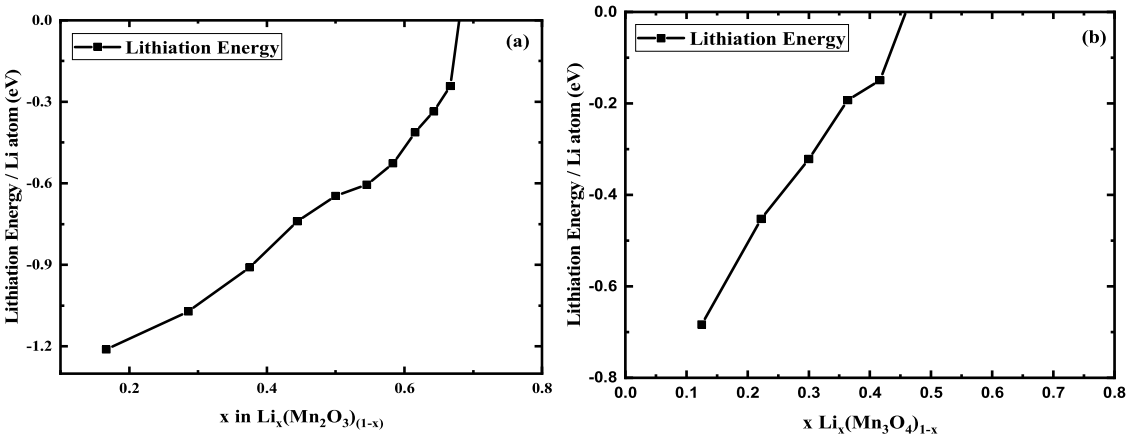

Figure 8. Estimated values of lithium lithiation energy as a function of lithium concentrations in the host matrix: (a) Mn_2O_3 and (b) Mn_3O_4.

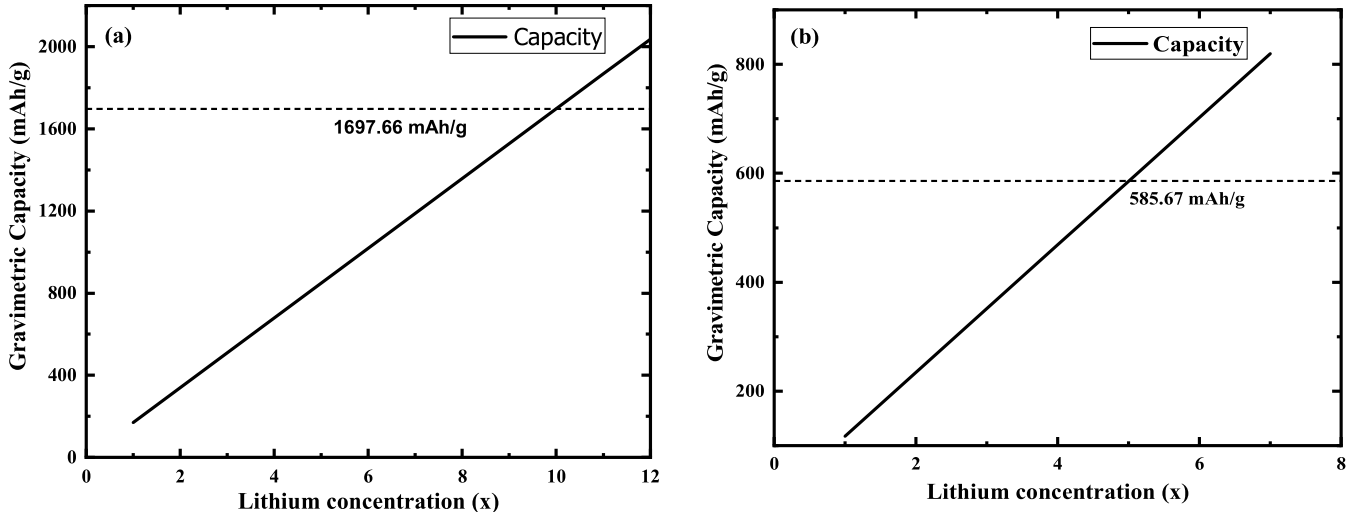

Figure 9. Gravimetric capacity of (a) Mn_2O_3 and (b) Mn_3O_4 as a function of Li concentration.

https://doi.org/10.1021/acsomega.3c06913
ACS Omega 2024, 9, 2457−2467

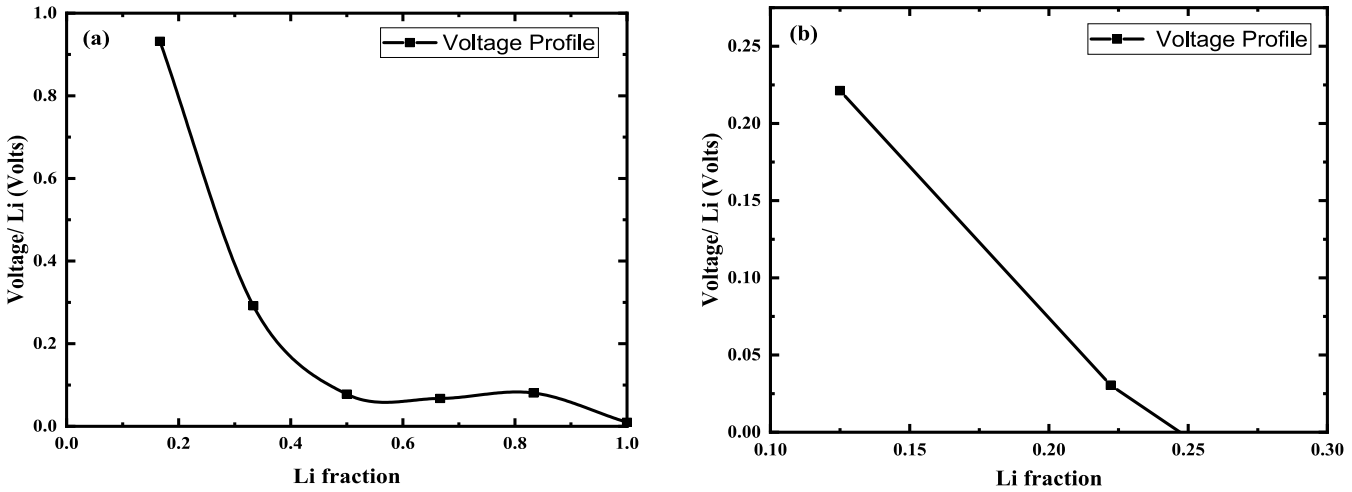

Figure 10. Voltage profile of (a) Mn_2O_3 and (b) Mn_3O_4 anode matrices as a function of Li absorption.

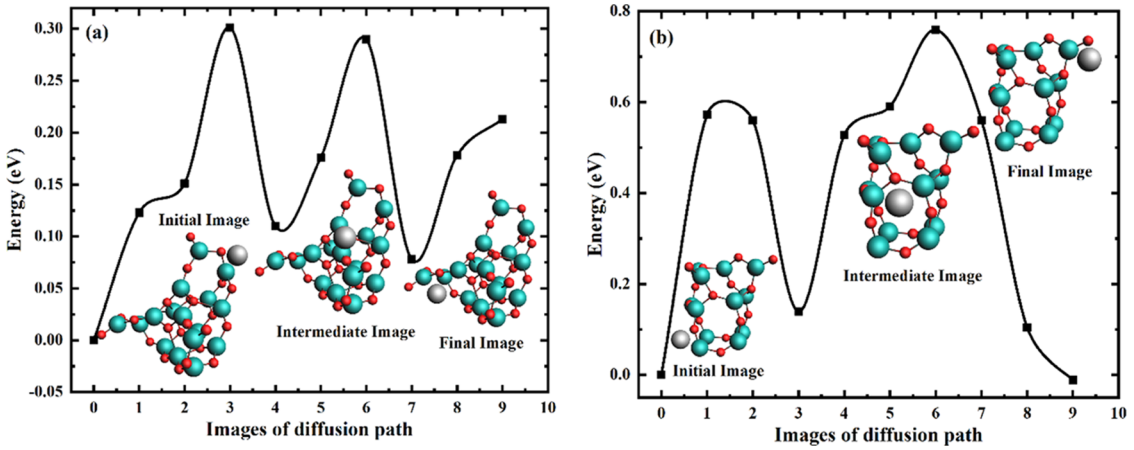

Figure 11. Cl-NEB simulations highlighting Li migration pathways in the host: (a) Mn_2O_3 with an energy barrier of 0.30 eV and (b) Mn_3O_4 with 0.75 eV.

Table 1. Comparison of Current Work with Potential Anode Materials Having Special Characteristics Necessary for LIBs

anode materials	adsorption energy (eV)	gravimetric capacity (mAh g^{-1})	open circuit voltage/lithium (OCV)	transition energy barrier (eV)	refs
Mn_2O_3	−0.24	1697.66	0.93	0.30*	this work
Mn_3O_4	−0.14	585.67	0.22	0.75*	this work
graphite	---	372	2.2−0.16	-----	50
Mn_2C	−1.93	879	0.05	-----	51
PNT	2.22	432	---	0.086	52
SIS	−0.44	446	---	0.31	53
Mo_2C	−0.26	526	---	0.015	54
Fe_2O_3	---	1293	---	-----	55
Co_3O_4/RGO	---	96.63	---	-----	56
V_2O_5	---	527	0.1−3	-----	57
FeV_2O_4	---	97	---	-----	58

observed up to 10 Li atoms and 5 Li atoms, respectively, but in graphite with a 372 mAh g^{-1} capacity,[48] the reaction persisted exothermic up to 5 Li atoms. It has been observed that in graphite, charge does not transfer after 5 Li intercalation; however, in the instance of Mn_2O_3, the intercalated Li transported charge up to 10 Li atoms. The fact that Mn_2O_3 and Mn_3O_4 have high capacities, i.e., 4.5 and 1.5 times higher than that of graphite, respectively, suggests that our proposed material is suitable for LIBs.

3.6.2. Voltage Profiling. The voltage profile is useful for assessing the electrode performance in LIBs. Equation 4 is used to determine how the intercalation voltage varies with varying lithium concentrations, and the resulting voltage profile is shown in Figure 10. The maximum calculated values of the Li insertion voltage per Li are 0.93 V for Mn_2O_3 and 0.22 V for Mn_3O_4. The results are consistent with the literature reported.[49]

3.6.3. Transition Energy Barrier. In order to further shed light on the lithiation/delithiation process, it is vital to explore

https://doi.org/10.1021/acsomega.3c06913
ACS Omega 2024, 9, 2457−2467

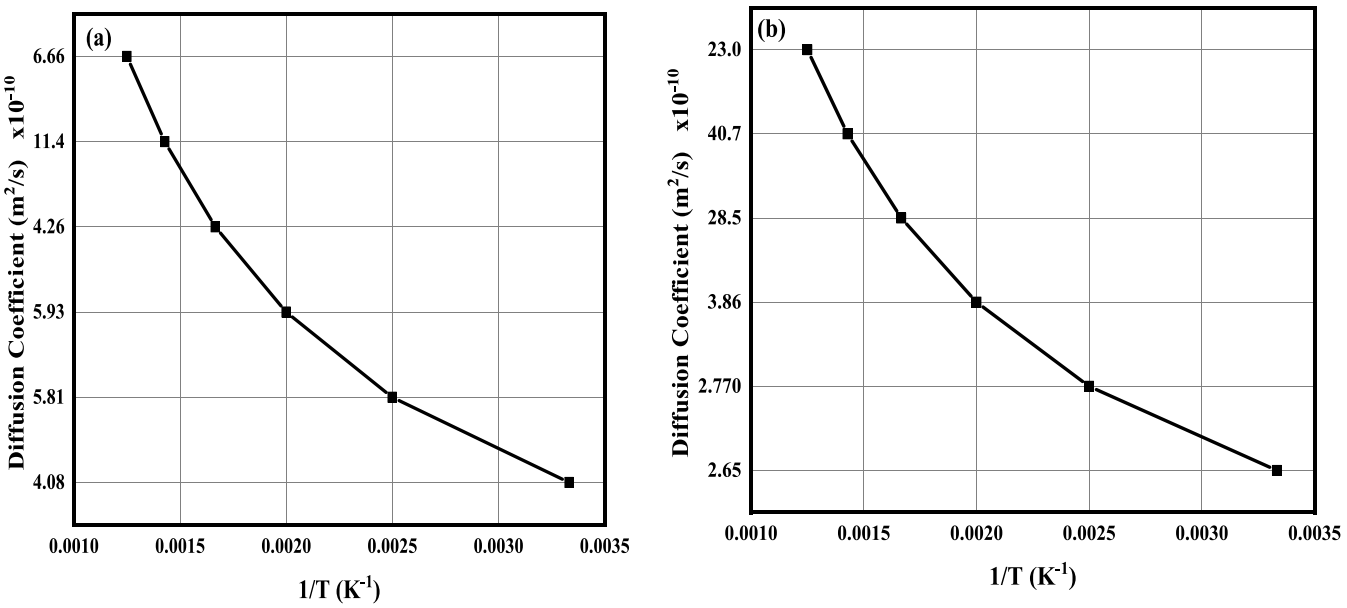

Figure 12. Calculated diffusion coefficient of anode materials: (a) Mn_2O_3 and (b) Mn_3O_4 for application in LIBs at different temperatures.

Li routes in the host and to calculate the energy barrier as the ligand moves through Mn_2O_3 and Mn_3O_4. The transition barrier is critical in determining how much energy is needed to charge the LIB. In order to calculate energy losses and the lowest energy barrier, CI-NEB calculations were used in each of the pathways depicted in Figure 11. In our simulations, we have taken different transition pathways but reported only two pathways that exhibited minimum energy barriers of 0.30 eV for Mn_2O_3 and 0.75 eV for Mn_3O_4. The transition energy barrier in the case of Mn_2O_3 is lower than that of the commercially available graphite anode (0.40 eV).[50]

3.6.4. Diffusion Coefficient. The study of lithium diffusion in Mn_2O_3 and Mn_3O_4 matrices is important when evaluation of the rate capability of lithium-ion batteries (LIBs) is taken into account. The comparison of the values calculated in this work and the reported literature is given in Table 1.

We conducted diffusion coefficient calculations (Figure 12) for lithium diffusion in Mn_2O_3 and Mn_3O_4 across a broad temperature range spanning from 300 to 800 K, which involves molecular dynamics (MD) simulations, utilizing the NVT ensemble along with a Berendsen thermostat.[59,60]

The mean square displacement (MSD) for the materials under study was determined using eqs 5 and 6. Generally, diffusion coefficients tend to increase with temperature until the solid reaches its melting point. The ease of ionic diffusion hinges on the interactions between diffusing ions and the host atoms. Trajectory analysis indicated slower diffusion at lower temperatures, attributed to the stronger bonding of Li with host atoms.[61−64] It appears that the interaction is enhanced with an increase in temperature, which activates the diffusion process to produce faster diffusion. Specifically, in the case of Mn_2O_3, the diffusion coefficient is found to be increased from 4.26×10^{-10} to 11.4×10^{-9} m^2/s with an increase in temperature from 600 to 700 K. On the other hand, in the case of Mn_3O_4, the diffusion coefficient appeared to have significantly increased from 3.86×10^{-10} to 4.0×10^{-9} m^2 s^{-1} with an increase in temperature from 500 to 700 K. These materials exhibited a higher diffusion coefficient when compared to commercially available graphite having the value as 4.43×10^{-9} to 5.24×10^{-10} cm^2 s^{-1}.[65]

4. SUMMARY

The potential of Mn_2O_3 and Mn_3O_4 as anode materials to be used in LIBs was examined in detail using first-principles methods. The findings revealed the capacity of 1697.66 mAh g^{-1} for Mn_2O_3, which points to its worth for use as an anode in LIBs without undergoing any structural change in comparison to Mn_3O_4, which exhibited a capacity of 585.67 mAh g^{-1}. The open circuit voltages per Li are found as 0.93 and 0.22 eV for Mn_2O_3 and Mn_3O_4, respectively. The intercalation process is exothermic until 10 Li insertion in the host Mn_2O_3 and 5 Li in host Mn_3O_4 because charge transfer only occurs when Li atoms are very close to the host structure. An analysis of the lithium transition energy barrier reveals the route of Li within the host structure. Cl-NEB shows that the Li transition barrier in the host Mn_2O_3 is 0.30 and 0.75 eV for Mn_3O_4. The phase change study reveals that an increase in temperature from 950 K causes a change in phase from Mn_3O_4 to Mn_2O_3. In the case of Mn_2O_3, the diffusion coefficient increased from 4.26×10^{-10} to 1.14×10^{-9} m^2 s^{-1} as the temperature was increased from 600 to 700 K. For Mn_3O_4, the diffusion coefficient significantly increased from 3.86×10^{-10} to 4.0×10^{-9} m^2 s^{-1} when the temperature was increased from 500 to 700 K. The study revealed high specific capacity, low Li diffusion energy barrier, and low open circuit voltage for Mn_2O_3-based anodes for use in LIBs.

■ ASSOCIATED CONTENT

Supporting Information

The Supporting Information is available free of charge at https://pubs.acs.org/doi/10.1021/acsomega.3c06913.

Description of experiments; experimental validation of phase change; TGA/DSC analysis; XRD analysis; and SEM analysis (PDF)

■ AUTHOR INFORMATION

Corresponding Author

Abdul Majid − *Department of Physics, University of Gujrat, Gujrat 50700, Pakistan;* orcid.org/0000-0003-0402-4838; Email: abdulmajid40@uog.edu.pk

https://doi.org/10.1021/acsomega.3c06913
ACS Omega 2024, 9, 2457−2467

Authors

Hira Batool − *Department of Physics, University of Gujrat, Gujrat 50700, Pakistan*

Sheraz Ahmad − *Department of Physics, University of Gujrat, Gujrat 50700, Pakistan*

Adil Mubeen − *Department of Physics, University of Gujrat, Gujrat 50700, Pakistan;* orcid.org/0000-0003-3575-6556

Mohammad Alkhedher − *Mechanical and Industrial Engineering Department, Abu Dhabi University, Abu Dhabi 59911, United Arab Emirates*

Waseem Sharaf Saeed − *Department of Restorative Dental Sciences, College of Dentistry, King Saud University, Riyadh 11545, Saudi Arabia;* orcid.org/0000-0002-5254-5665

Ahmad Abdulaziz Al-Owais − *Chemistry Department, College of Science, King Saud University, Riyadh 11451, Saudi Arabia*

Aqeel Afzal − *Ryan Institute's Centre for Climate and Air Pollution Studies, Physics, School of Natural Sciences, University of Galway, Galway H91 TK33, Ireland*

Complete contact information is available at: https://pubs.acs.org/10.1021/acsomega.3c06913

Notes

The authors declare no competing financial interest.

■ ACKNOWLEDGMENTS

The authors would like to extend their sincere appreciation to the Researchers Supporting Project number (RSPD2024R755), King Saud University, Riyadh, Saudi Arabia.

■ REFERENCES

(1) Sarkar, S.; Roy, S.; Hou, Y.; et al. Recent Progress in Amorphous Carbon-Based Materials for Anodes of Sodium-Ion Batteries: Synthesis Strategies, Mechanisms, and Performance. *ChemSusChem* **2021**, *14* (18), 3693−3723, DOI: 10.1002/cssc.202101270.

(2) Khan, M. M.; Alkhedher, M.; Ramadan, M.; Ghazal, M. Hybrid PCM-based thermal management for lithium-ion batteries: Trends and challenges. *J. Energy Storage* **2023**, *73*, No. 108775.

(3) Shen, S.; Chen, Y.; Zhou, J.; Zhang, H.; et al. Microbe-Mediated Biosynthesis of Multidimensional Carbon-Based Materials for Energy Storage Applications. *Adv. Energy Mater.* **2023**, *13*, No. 2204259, DOI: 10.1002/aenm.202204259.

(4) Kamali-Heidari, E.; Kamyabi-Gol, A.; Sohi, M. H.; Ataie, A. Electrode materials for lithium ion batteries: a review. *J. Ultrafine Grained Nanostruct. Mater.* **2018**, *51* (1), 1−12.

(5) Yang, S.; Feng, X.; Ivanovici, S.; et al. Fabrication of graphene-encapsulated oxide nanoparticles: towards high-performance anode materials for lithium storage. *Angew. Chem.* **2010**, *122* (45), 8586−8589.

(6) Li, W.-Y.; Xu, L.-N.; Chen, J. Co3O4 nanomaterials in lithium-ion batteries and gas sensors. *Adv. Funct. Mater.* **2005**, *15* (5), 851−857.

(7) Chan, C. K.; Zhang, X. F.; Cui, Y. High capacity Li ion battery anodes using Ge nanowires. *Nano Lett.* **2008**, *8* (1), 307−309.

(8) Fatima, A.; Majid, A.; Haider, S.; Akhtar, M. S.; Alkhedher, M. First principles study of layered silicon carbide as anode in lithium ion battery. *Int. J. Quantum Chem.* **2022**, *122* (11), No. e26895.

(9) Mahek, M. K.; Alkhedher, M.; Ramadan, M.; Abdelkareem, M. A.; Olabi, A. G. A Comparative Study of Active, Passive, and Hybrid Thermal Management Systems for Li-Ion Batteries: Performance Analysis. *Adv. Sci. Technol.* **2023**, *133*, 45−52, DOI: 10.4028/p-p12kww.

(10) Choi, N. S.; Chen, Z.; Freunberger, S. A.; et al. Challenges facing lithium batteries and electrical double-layer capacitors. *Angew. Chem., Int. Ed.* **2012**, *51* (40), 9994−10024.

(11) Koo, B.; Xiong, H.; Slater, M. D.; et al. Hollow iron oxide nanoparticles for application in lithium ion batteries. *Nano Lett.* **2012**, *12* (5), 2429−2435.

(12) Wang, X.; Wu, X.; Guo, Y.; et al. Synthesis and lithium storage properties of Co3O4 nanosheet-assembled multishelled hollow spheres. *Adv. Funct. Mater.* **2010**, *20* (10), 1680−1686.

(13) Hatchard, T. D.; Dahn, J. R. In situ XRD and electrochemical study of the reaction of lithium with amorphous silicon. *J. Electrochem. Soc.* **2004**, *151* (6), No. A838, DOI: 10.1149/1.1739217.

(14) ArunaBharathi, M.; Sushama, M.; Rao, K. V.; Rao, G. V. Experimentaland computational analysis of metal oxide nanomaterials for lithium-ion batteries. *Mater. Today: Proc.* **2023**, *92*, 1591−1596, DOI: 10.1016/j.matpr.2023.06.073.

(15) Hassan, A. S.; Navulla, A.; Meda, L.; et al. Molecular mechanisms for the lithiation of ruthenium oxide nanoplates as lithium-ion battery anode materials: an experimentally motivated computational study. *J. Phys. Chem. C* **2015**, *119* (18), 9705−9713, DOI: 10.1021/jp5123536.

(16) Bhattacharya, P.; Nasybulin, E. N.; Engelhard, M. H.; et al. Dendrimer-encapsulated ruthenium oxide nanoparticles as catalysts in lithium-oxygen batteries. *Adv. Funct. Mater.* **2014**, *24* (47), 7510−7519, DOI: 10.1002/adfm.201402701.

(17) Navulla, A.; Stevens, G.; Kovalenko, I.; Meda, L. Hierarchical columnar RuO2 nanoplates and their Improved cycle life performance at high capacity. *J. Phys. Chem. C* **2014**, *118* (25), 13382−13386, DOI: 10.1021/jp5012632.

(18) Gurmesa, G. S.; Benti, N. E.; Chaka, M. D.; et al. Fast 3D-lithium-ion diffusion and high electronic conductivity of Li 2 MnSiO 4 surfaces for rechargeable lithium-ion batteries. *RSC Adv.* **2021**, *11* (16), 9721−9730.

(19) Perdew, J. P.; Burke, K.; Ernzerhof, M. Generalized gradient approximation made simple. *Phys. Rev. Lett.* **1996**, *77* (18), No. 3865, DOI: 10.1103/PhysRevLett.77.3865.

(20) Allam, O.; Cho, B. W.; Kim, K. C.; et al. Application of DFT-based machine learning for developing molecular electrode materials in Li-ion batteries. *RSC Adv.* **2018**, *8* (69), 39414−39420.

(21) Lee, Y.-T.; Kuo, C.-T.; Yew, T.-R. Investigation on the voltage hysteresis of Mn3O4 for lithium-ion battery applications. *ACS Appl. Mater. Interfaces* **2021**, *13* (1), 570−579.

(22) Reddy, M. V.; Rao, G. S.; Chowdari, B. Metal oxides and oxysalts as anode materials for Li ion batteries. *Chem. Rev.* **2013**, *113* (7), 5364−5457.

(23) Cao, K.; Jin, T.; Yang, L.; et al. Recent progress in conversion reaction metal oxide anodes for Li-ion batteries. *Mater. Chem. Front.* **2017**, *1* (11), 2213−2242.

(24) Banerjee, A.; Shilina, Y.; Ziv, B.; et al. On the oxidation state of manganese ions in Li-ion battery electrolyte solutions. *J. Am. Chem. Soc.* **2017**, *139* (5), 1738−1741.

(25) Neelapala, S. D.; Patnaik, H.; Dasari, H. Enhancement of soot oxidation activity of manganese oxide (Mn2O3) through doping by the formation of Mn1. 9M0. 1O3−δ (M= Co, Cu, and Ni). *Asia-Pac. J. Chem. Eng.* **2018**, *13* (5), No. e2234, DOI: 10.1002/apj.2234.

(26) Raj, B. G. S.; Asiri, A. M.; Wu, J. J.; et al. Synthesis of Mn3O4 nanoparticles via chemical precipitation approach for supercapacitor application. *J. Alloys Compd.* **2015**, *636*, 234−240.

(27) Kim, H.; Lim, K.; Yoon, G.; et al. Exploiting Lithium−Ether Co-Intercalation in Graphite for High-Power Lithium-Ion Batteries. *Adv. Energy Mater.* **2017**, *7* (19), No. 1700418, DOI: 10.1002/aenm.201700418.

(28) Sethuraman, V. A.; Hardwick, L. J.; Srinivasan, V.; et al. Surface structural disordering in graphite upon lithium intercalation/deintercalation. *J. Power Sources* **2010**, *195* (11), 3655−3660.

(29) Sakai, Y.; Oshiyama, A. Electron doping through lithium intercalation to interstitial channels in tetrahedrally bonded SiC. *J. Appl. Phys.* **2015**, *118* (17), No. 175704.

(30) Xu, J.; Mahmood, J.; Dou, Y.; et al. 2D Frameworks of C2N and C3N as New Anode Materials for Lithium-Ion Batteries. *Adv. Mater.* **2017**, *29* (34), No. 1702007.
(31) Wu, Y.; Wang, S.; Xie, Y.; et al. Highly stable TiOF monolayer as anode material for the applications of Li/Na-ion batteries. *Appl. Surf. Sci.* **2022**, *574*, No. 151296, DOI: 10.1016/j.apsusc.2021.151296.
(32) Bhauriyal, P.; Mahata, A.; Pathak, B. Graphene-like carbon−nitride monolayer: a potential anode material for Na-and K-ion batteries. *J. Phys. Chem. C* **2018**, *122* (5), 2481−2489.
(33) Ehteshami, N.; Eguia-Barrio, A.; de Meatza, I.; et al. Adiponitrile-based electrolytes for high voltage, graphite-based Li-ion battery. *J. Power Sources* **2018**, *397*, 52−58.
(34) Coates, A. S.; Winer, E. P.; Goldhirsch, A.; Gelber, R. D.; et al. Tailoring therapies—improving the management of early breast cancer: St Gallen International Expert Consensus on the Primary Therapy of Early Breast Cancer 2015. *Ann. Oncol.* **2015**, *26* (8), 1533−1546, DOI: 10.1093/annonc/mdv221.
(35) Mathiesen, N. R.; Jónsson, H.; Vegge, T.; et al. R-neb: Accelerated nudged elastic band calculations by use of reflection symmetry. *J. Chem. Theory Comput.* **2019**, *15* (5), 3215−3222.
(36) Nobile, M. S.; Cazzaniga, P.; Besozzi, D.; et al. Fuzzy Self-Tuning PSO: A settings-free algorithm for global optimization. *Swarm Evol. Comput.* **2018**, *39*, 70−85.
(37) Barcaro, G.; Sementa, L.; Carravetta, V.; et al. Experimental and theoretical elucidation of catalytic pathways in TiO 2-initiated prebiotic polymerization. *Phys. Chem. Chem. Phys.* **2019**, *21* (10), 5435−5447.
(38) Apte, S. K.; Naik, S. D.; Sonawane, R. S.; Kale, B. B.; et al. Nanosize Mn3O4 (Hausmannite) by microwave irradiation method. *Mater. Res. Bull.* **2006**, *41* (3), 647−654, DOI: 10.1016/j.materresbull.2005.08.028.
(39) Savin, A.; Nesper, R.; Wengert, S.; Fässler, T. F. ELF: The electron localization function. *Angew. Chem., Int. Ed. Engl.* **1997**, *36* (17), 1808−1832, DOI: 10.1002/anie.199718081.
(40) Impacts of structural downscaling of inorganic molecular crystals - A DFT study of Sb2O3
(41) Chase, M. W.; N.I.S. Organization. *NIST-JANAF Thermochemical Tables*; American Chemical Society: Washington, DC, 1998; Vol. *9*.
(42) Bai, Z.; Sun, B.; Fan, N.; et al. Branched mesoporous Mn3O4 nanorods: facile synthesis and catalysis in the degradation of methylene blue. *Chem. - Eur. J.* **2012**, *18* (17), 5319−5324, DOI: 10.1002/chem.201102944.
(43) Ulutas, C.; Erken, O.; Gunes, M.; Gumus, C. Effect of annealing temperature on the physical properties of Mn3O4 thin film prepared by chemical bath deposition. *Int. J. Electrochem. Sci.* **2016**, *11*, 2835−2845, DOI: 10.1016/s1452-3981(23)16144-x.
(44) Dang, H. T.; Ai, X.; Millis, A. J.; et al. Density functional plus dynamical mean-field theory of the metal-insulator transition in early transition-metal oxides. *Phys. Rev. B* **2014**, *90* (12), No. 125114.
(45) May, K. J.; Kolpak, A. M. Improved description of perovskite oxide crystal structure and electronic properties using self-consistent Hubbard U corrections from ACBN0. *Phys. Rev. B* **2020**, *101* (16), No. 165117.
(46) Choudhary, K.; Zhang, Q.; Reid, A. C. E.; Chowdhury, S.; et al. Computational screening of high-performance optoelectronic materials using OptB88vdW and TB-mBJ. formalisms. *Sci. Data* **2018**, *5* (1), No. 180082, DOI: 10.1038/sdata.2018.82.
(47) Hansson, T.; Oostenbrink, C.; van Gunsteren, W. Molecular dynamics simulations. *Curr. Opin. Struct. Biol.* **2002**, *12* (2), 190−196, DOI: 10.1016/s0959-440x(02)00308-1.
(48) Mortazavi, B.; Dianat, A.; Cuniberti, G.; et al. Application of silicene, germanene and stanene for Na or Li ion storage: A theoretical investigation. *Electrochim. Acta* **2016**, *213*, 865−870.
(49) Gu, X.; Yue, J.; Li, L.; et al. General synthesis of MnOx (MnO2, Mn2O3, Mn3O4, MnO) hierarchical microspheres as lithium-ion battery anodes. *Electrochim. Acta* **2015**, *184*, 250−256.
(50) Wang, Z.; Fu, Y.; Zhang, Z.; Yuan, S.; et al. Application of stabilized lithium metal powder (SLMP) in graphite anode−a high efficient prelithiation method for lithium-ion batteries. *J. Power Sources* **2014**, *260*, 57−61, DOI: 10.1016/j.jpowsour.2014.02.112.
(51) Zhou, Y.; Zu, X. Mn2C sheet as an electrode material for lithium-ion battery: A first-principles prediction. *Electrochim. Acta* **2017**, *235*, 167−174.
(52) Cao, J.; Shi, J.; Hu, Y.; et al. Lithium ion adsorption and diffusion on black phosphorene nanotube: A first-principles study. *Appl. Surf. Sci.* **2017**, *392*, 88−94.
(53) Jiang, H.; Zhao, T.; Liu, M.; et al. Two-dimensional SiS as a potential anode material for lithium-based batteries: A first-principles study. *J. Power Sources* **2016**, *331*, 391−399.
(54) Aarons, J.; Sarwar, M.; Thompsett, D.; Skylaris, C.-K. Perspective: Methods for large-scale density functional calculations on metallic systems. *J. Chem. Phys.* **2016**, *145* (22), No. 220901, DOI: 10.1063/1.4972007.
(55) Aslam, J.; Wang, Y. Metal Oxide Wrapped by Reduced Graphene Oxide Nanocomposites as Anode Materials for Lithium-Ion Batteries. *Nanomaterials* **2023**, *13* (2), No. 296, DOI: 10.3390/nano13020296.
(56) Dong, L.; Wang, Z.; Li, Y.; Jin, C.; et al. Spinel-Structured, Multi-Component Transition Metal Oxide (Ni,Co,Mn)Fe2O4−x as Long-Life Lithium-Ion Battery Anode Material. *Batteries* **2023**, *9* (1), No. 54, DOI: 10.3390/batteries9010054.
(57) Yan, B.; Li, X.; Fu, X.; et al. An elaborate insight of lithiation behavior of V2O5 anode. *Nano Energy* **2020**, *78*, No. 105233.
(58) Maggay, I. V. B.; De Juan, L. M. Z.; Lu, J. S.; et al. Electrochemical properties of novel FeV(2)O(4) as an anode for Na-ion batteries. *Sci. Rep.* **2018**, *8* (1), No. 8839, DOI: 10.1038/s41598-018-27083-z.
(59) Yi, T.-F.; Wei, T.-T.; Li, Y.; et al. Efforts on enhancing the Li-ion diffusion coefficient and electronic conductivity of titanate-based anode materials for advanced Li-ion batteries. *Energy Storage Mater.* **2020**, *26*, 165−197, DOI: 10.1016/j.ensm.2019.12.042.
(60) Azmat, M.; Majid, A.; Alkhedher, M.; Haider, S.; Akhtar, M. S. A first-principles study on two-dimensional tetragonal samarium nitride as a novel photocatalyst for hydrogen production. *Int. J. Hydrogen Energy* **2023**, *48*, 30732−30740, DOI: 10.1016/j.ijhydene.2023.04.248.
(61) Zabara, M. A.; Katırcı, G.; Ülgüt, B. Operando Investigations of the Interfacial Electrochemical Kinetics of Metallic Lithium Anodes via Temperature-Dependent Electrochemical Impedance Spectroscopy. *J. Phys. Chem. C* **2022**, *126* (27), 10968−10976.
(62) Zhakupbekova, A.; Baimatova, N.; Kenessov, B. A critical review of vacuum-assisted headspace solid-phase microextraction for environmental analysis. *Trends Environ. Anal. Chem.* **2019**, *22*, No. e00065, DOI: 10.1016/j.teac.2019.e00065.
(63) Savadogo, M.; Soro, B.; Konate, R.; Sourabié, I.; et al. Temperature Effect on Light Concentration Silicon Solar Cell's Operating Point and Conversion Efficiency. *Smart Grid Renewable Energy* **2020**, *11* (5), 61−72, DOI: 10.4236/sgre.2020.115005.
(64) Ahmed, S.; Alkhedher, M.; Isa, M.; Majid, A. First Principles Study of Layered CrGeTe3 as Lithium Intercalation Compound. *J. Electrochem. Soc.* **2022**, *169* (4), No. 040557.
(65) Guo, H.-j.; LI, X.-h.; Zhang, X.-m.; et al. Diffusion coefficient of lithium in artificial graphite, mesocarbon microbeads, and disordered carbon. *New Carbon Mater.* **2007**, *22* (1), 7−10, DOI: 10.1016/S1872-5805(07)60006-7.

https://doi.org/10.1021/acsomega.3c06913
ACS Omega 2024, 9, 2457−2467